Toward Noninvasive Quantification of Brain Radioligand Binding by Combining Electronic Health Records and Dynamic PET Imaging Data

Arthur Mikhno, Francesca Zanderigo, R. Todd Ogden, J. John Mann, Elsa D. Angelini, Andrew F. Laine, and Ramin V. Parsey

***Abstract*—Quantitative analysis of positron emission tomography (PET) brain imaging data requires a metabolite-corrected arterial input function (AIF) for estimation of distribution volume and related outcome measures. Collecting arterial blood samples adds risk, cost, measurement error, and patient discomfort to PET studies. Minimally invasive AIF estimation is possible with simultaneous estimation (SIME), but at least one arterial blood sample is necessary. In this study, we describe a noninvasive SIME (nSIME) approach that utilizes a pharmacokinetic input function model and constraints derived from machine learning applied to an electronic health record database consisting of "long tail" data (digital records, paper charts, and handwritten notes) that were collected ancillary to the PET studies. We evaluated the performance of nSIME on 95 [^{11}C]DASB PET scans that had measured AIFs. The results indicate that nSIME is a promising alternative to invasive AIF measurement. The general framework presented here may be expanded to other metabolized radioligands, potentially enabling quantitative analysis of PET studies without blood sampling. A glossary of technical abbreviations is provided at the end of this paper.**

***Index Terms*—Arterial input function (AIF), electronic health record (EHR), positron emission tomography (PET) imaging.**

I. Introduction

POSITRON emission tomography (PET) uses radioactively tagged probes (radioligands) for the *in vivo* quantification of blood flow, metabolism, protein distribution, gene expression, and drug target occupancy in the brain. Fully quantitative analysis of PET data requires both the arterial input function (AIF) that describes the amount of radioligand available for diffusion into the brain, and the tissue time-activity curves (TACs) derived from dynamic PET images. Kinetic modeling is then performed to estimate important outcome measures of radioligand distribution and binding [1]. To measure the AIF, typically a catheter is inserted into the radial artery at a subjects' wrist to sample blood for the duration of the PET scan. After centrifugation, the total radioactivity concentration of radioligand in the arterial plasma (TP) is measured in each blood sample. If the body metabolizes the radioligand, the parent fraction (PF) of unmetabolized radioligand in the plasma is assayed from a subset of the blood samples. After fitting PF using a metabolite model, the input function is calculated as $\mathrm{AIF} : y = \mathrm{TP} \times \mathrm{PF}$, which reflects the concentration y of radioligand in plasma that is available to enter the target tissue.

Utilizing the AIF and the TACs, PET imaging can be used to estimate outcome measures related to the "binding potential" of a radioligand to its target. In particular, one estimate of binding potential BP_F is defined as: $\mathrm{BP}_F = B_{\mathrm{avail}}/K_D = (V_T - V_{\mathrm{ND}})/f_P$, where B_{avail} is the concentration of available receptors, $1/K_D$ is the radioligand affinity to the target, V_T is the radioligand "volume of distribution" or volume of radioligand in tissue relative to plasma, V_{ND} is the radioligand "volume of distribution" in a tissue devoid of the target (i.e., fraction of binding not specific to the target of interest), and f_P is the free fraction of the radioligand in plasma. V_T and V_{ND} are estimated from kinetic modeling of the region TACs and the AIF, while f_P can be assayed in additional blood samples collected prior to radioligand injection. When f_{P} is not available, or cannot be measured reliably, two other variants binding potential can be calculated: $\mathrm{BP}_P = f_P \mathrm{BP}_F = (V_T - V_{\mathrm{ND}})$ and $\mathrm{BP}_{\mathrm{ND}} = f_{\mathrm{ND}} BP_F = (V_T - V_{\mathrm{ND}})/V_{\mathrm{ND}}$, where f_{ND} is the free fraction of the radioligand in a tissue devoid of target.

Thus, quantification of PET data requires arterial blood sampling to estimate the AIF and to calculate the outcome measures related to the "binding potential" of the radioligand to its target (i.e., BP_P or $\mathrm{BP}_{\mathrm{ND}}$). While arterial sampling is routinely done in research studies, it is invasive, necessitates specific technical expertise, exposes clinical personnel to radiation, involves laboratory analysis costs, significant measurement error, and strongly discourages subject participation in PET studies. If the patient refuses an arterial line, or if arterial cannulation or blood assay fails, the entire study may be dropped from data analysis leaving expensive PET images that cannot be interpreted or

Manuscript received October 15, 2014; revised January 5, 2015 and March 6, 2015; accepted March 14, 2015. Date of publication March 24, 2015; date of current version July 23, 2015. This work was supported by the National Institute of Mental Health (NIMH) F31 Predoctoral Fellowship (1F31MH095338) and NIMH Grants MH040695 and MH062185, and the National Center for Advancing Translational Sciences, National Institutes of Health, Grant TL1 TR000082.

A. Mikhno, E. D. Angelini, and A. F. Laine are with the Department of Biomedical Engineering, Columbia University, New York, NY 10027 USA (e-mail: am2679@columbia.edu; ea179@columbia.edu; AL418@columbia.edu).

F. Zanderigo is with the Department of Psychiatry, Columbia University and the Division of Molecular Imaging and Neuropathology, New York Psychiatric Institute, New York, NY 10021 USA (e-mail: zanderi@nyspi.columbia.edu).

R. Todd Ogden is with the Department of Biostatistics, Columbia University, New York, NY 10032 USA (e-mail: to166@columbia.edu).

J. J. Mann is with the Department of Psychiatry, Columbia University, New York, NY 10032 USA (e-mail: jjm@columbia.edu).

R. V. Parsey is with the Department of Psychiatry, Stony Brook University, Stony Brook, NY 11794 USA (e-mail: Ramin.Parsey@stonybrookmedicine.edu).

Color versions of one or more of the figures in this paper are available online at http://ieeexplore.ieee.org.

Digital Object Identifier 10.1109/JBHI.2015.2416251

2168-2194 © 2015 IEEE. Translations and content mining are permitted for academic research only. Personal use is also permitted, but republication/redistribution requires IEEE permission. See http://www.ieee.org/publications_standards/publications/rights/index.html for more information.

analyzed. Even when these challenges are anticipated, it may not always be possible to perform arterial blood sampling, such as with vulnerable populations (e.g., elderly, cancer patients), those with movement disorders (e.g., people affected by Parkinson's disease) or in a combined magnetic resonance imaging (MRI) and PET scanner due to magnetic interference. Even when blood samples can be obtained, fitting of TP and PF can be challenging due to inherent noise present in the blood measurements, and complex radioligand kinetics such as "lung trapping" that require adapting and validating a metabolite model [2]. Finally, and most commonly, arterial sampling is impractical in a clinical setting, hindering adoption of quantitative PET outcome measures for clinical use.

The last decade has brought a considerable effort to develop AIF estimation techniques [3] that can be broadly categorized as noninvasive (i.e., without blood samples), such as "reference tissue" and population-based approaches, and minimally invasive (i.e., with few blood samples), such as image-derived input functions (IDIF).

Reference tissue methods use only imaging data to estimate kinetic parameters of tissue TACs, based on the specification that a valid reference region devoid of the target (e.g., receptor or protein of interest) exists and can be identified [4]. This approach allows estimation of $\mathrm{BP_{ND}}$ only. For many radioligands currently employed in brain studies, a reference region truly devoid of the target cannot be identified or the region commonly used as a reference actually has measurable specific binding. Even when a reference region is identifiable, there may be high bias and variance in $\mathrm{BP_{ND}}$ values calculated with the reference tissue methods when compared to using the AIF, as is the case with [^{11}C]-PK11195 (targeting microglia) [5], and [^{11}C]ABP (targeting the metabotropic glutamate receptor subtype 5) [6]. Population-based approaches define a template AIF, typically generated from AIF values derived from blood samples collected across several studies with the same radioligand. The template AIF is applied to new subjects after adjusting by a scaling factor based on their injected dose (ID) and body mass [7], or based on cerebellar activity [8]. Even when the scaling factor is derived invasively from arterial blood samples, the shape of the AIF can vary greatly between subjects. To date, population approaches had limited success with few radioligands (e.g., [^{18}F]FDG [8], [^{11}C]PIB [9]).

With these limitations in mind, most efforts have focused on developing minimally invasive IDIF methods that can yield individualized estimates of the AIF. These approaches are based on estimating the AIF from dynamic PET imaging data. A common IDIF approach involves averaging the signal from a region of interest (ROI) placed over the carotid artery identified directly on PET images either manually [10], by automated segmentation techniques [11], or with the help of a coregistered MRI image [12]. Alternatively, clustering [13] or independent component analysis [14] can be used to extract the blood signal from blood vessels in the brain. The drawback of the aforesaid approaches is that they require at least one blood sample for scaling of the estimated AIF, and at least three or more samples for metabolite correction [3]. Another class of IDIF approaches is based on simultaneous estimation (SIME) of multiple TACs, with the underlying assumption that the AIF is the same for all ROIs. SIME exploits a parametric model for the unknown AIF and seeks to estimate model parameters simultaneously with the kinetic parameters related to the binding, while fitting several ROIs at the same time. Recent work has shown that SIME can recover the AIF using only a single arterial blood sample as an anchor (or constraint) that ensures model identifiability [15]. One more alternative for a "less" invasive IDIF is to measure TP and PF from venous blood sampling [3]. Drawing venous blood does not require arterial catheterization by trained personnel, making it more practical in research and clinical settings. For some radioligands, this substitution is nearly equivalent as with [^{18}F]FDG [10], [16] and [^{11}C]WAY [17]. The equivalence between arterial and venous blood must be determined separately for each radioligand and often does not hold. This procedure still requires considerable effort with regards to blood draws and the metabolite correction assay.

A totally noninvasive AIF estimation approach is needed to overcome the aforesaid challenges and drawbacks with existing IDIF techniques. Our proposed solution taps into the field of population pharmacokinetics and pharmacodynamics (PPKD) that focuses on predicting metabolite corrected blood levels of pharmaceutical compounds at various time points after injection. This is done by aggregating blood data from many subjects to determine what measures (e.g., age, body mass index (BMI), glomerular filtration rate, etc.) explain the variance in drug blood concentration [18]. Previous work suggests that combining supplementary information (e.g., weight, height, ID) with signal from cranial blood vessels improves IDIF-based AIF estimation [19]. However, this technique was developed for the radioligand [^{18}F]FDG for which metabolites are not present in the blood (i.e., $\mathrm{PF} = 1$). It is not clear whether such an approach could translate to radioligands that undergo significant metabolism.

In this study, we bridge PPKD and PET brain imaging by merging SIME with predicted constraints on the parameters of the AIF model that are derived from machine learning applied to electronic health record (EHR) data. We previously demonstrated the feasibility of using EHR data to predict the metabolite corrected radioligand blood concentration of a single blood sample [20]. Here, we develop an algorithm for noninvasively estimating the full AIF curve and validate it on brain PET data acquired with the radioligand [^{11}C]DASB that binds the serotonin transporter [21].

In this context, we designed a big-data analytics solution toward noninvasive PET quantification, handling two big-data challenges [22]: the first challenge was the low veracity of the "long tail" EHR records collected prior to the PET studies, largely recorded in handwritten notes, and not quality controlled. The second challenge was the wide variety of data, combining multimodal time-series PET/MRI images, blood measures, and static EHR measures from different statistical distributions.

II. Methodology

A. Subjects and Data

In a study approved by the Institute Review Board, PET and EHR data were obtained for 228 [^{11}C]DASB PET scans at the Kreitchman PET Center at the Columbia University Medical Center between 2004 and 2012. Health records consisted of

TABLE I
DESCRIPTIVE STATISTICS FOR DEMOGRAPHICS AND VITALS MEASURES

Variable	Mean (STD)	min	max
Age (years)	38 (12)	19	64
Weight (lb)	165 (41)	102	279
Height (in)	66 (3)	60	73
pre-scan Δt (h)	2.3 (1.2)	9	0.5
post-scan Δt (h)	4.9 (1.4)	1.9	7.8
BPs_pre (mmHg)	122 (17)	90	189
BPs_post	122 (17)	93	178
BPd_pre (mmHg)	75 (9)	53	107
BPd_post	76 (12)	54	128
HR_pre (beats/min)	72 (11)	45	100
HR_post	73 (12)	48	105

Heart rate (HR), systolic blood pressure (BPs) and diastolic blood pressure (BPd) were collected before (_pre) and after (_post) PET scan within the time interval Δt.

data collected prior to the PET scan date and included demographics (e.g., age, sex), clinical details (e.g., weight, vitals), clinical laboratory test results (e.g., blood chemistry, clinical blood counts, thyroid panel), and urinalysis (e.g., pH). Heart rate (HR) and blood pressure (BP) were obtained within a few hours before and/or after the PET scan. PET data included regional brain TACs, ID, injected mass, radioligand specific activity, and measured AIF based on full arterial blood sampling. Only 95 of 228 available [^{11}C]DASB PET scans had accompanying weight, height, HR, BP, and useable AIF data. All analysis presented here were conducted on these 95 [^{11}C]DASB PET scans, for which descriptive statistics are shown in Table I.

B. Vitals and Hemodynamic Related Variables

The HR was measured manually via radial pulse rate, systolic (BPs) and diastolic (BPd) BP measurements were obtained with a sphygmomanometer, before and after the PET scan. The aforesaid measures were manually transcribed from handwritten notes made on a PET protocol form by clinical technicians. Missing or illegible records were marked as "Not a Number" and discarded. Vital signs were not assessed at consistent times; they ranged from 9 to 1 h for pre-scan and from 2 to 8 h for postscan measurements. Therefore, variables that represent the "closest" and "average" vitals were also calculated. Summary statistics for vitals are shown in Table I.

The following hemodynamics related variables were also derived from HR and BP measures: mean arterial pressure (MAP), pulse pressure (PP) and a very simplified estimated cardiac output (eCO), using the assumption that PP is proportional to stroke volume [23].

C. Additional Derived Variables

The following variables were also derived from the age (A), weight (W), height (H), and hematocrit (Hct) of each subject: BMI, body surface area (BSA) using Mosteller's equation [24], estimated total blood volume (*e*TBV) using Nadler's equation [25], estimated total plasma volume (*e*TPV), defined as $e\mathrm{TPV} = e\mathrm{TBV} \cdot (1 - Hct)$, and estimated resting metabolic (*e*RMR) rate using Mifflin's equation [26]. The glomerular filtration rate (GFR) was estimated using two "Modification of Diet in Renal Disease" formulas [27]: the simplified version that uses blood creatinine level (*e*GFR) and a more complex version that incorporates blood urea nitrogen and albumin (*e*GFR5). Since the formulas are implicitly adjusted for BSA and reported as ml/min/1.73 m^2, two additional variants were calculated adjusting to each individual's BSA and dividing by 1.73 [28]. Other calculated standard clinical variables included osmolality gap, albumin corrected calcium, blood viscosity, anion gap, Bun:creatinine ratio, and plasma osmolality.

D. PET Image Acquisition and Processing

Brain PET acquisition and processing, as well as arterial blood analysis, were previously described in detail [2], [29]. Briefly, PET imaging was performed with the ECAT HR+ (Siemens/CTI, Knoxville, Tennessee). After a 10-min the transmission scan, between 5 and 20 mCi of [^{11}C]DASB was administered intravenously as a short infusion over 30 s. Emission data were collected for 100 min over 19 frames of increasing duration: 3×20 s, 3×1 min, 3×2 min, 2×5 min, and 8×10 min. Images were reconstructed to a 128×128 matrix (pixel size of 2.5 mm $\times$ 2.5 mm). PET images were motion corrected and coregistered to an accompanying 1.5T or a 3T MRI image. The TACs were obtained from seven manually traced ROIs on the MRI that were transferred to the coregistered PET scan. These ROIs were previously used for SIME with [^{11}C]DASB [15] and include: gray matter cerebellum, midbrain, amygdala, dorsal caudate, hippocampus, temporal lobe, and ventral striatum. Thirty-one arterial blood samples were collected during the PET scan. TP was measured from arterial plasma using a well counter after centrifugation. PF was calculated after measurement of plasma parent radioligand and plasma metabolites concentrations with a high-pressure liquid chromatography assay from a subset of these blood samples.

E. Estimation of the AIF

The discrete time course of the AIF can be described as: $y[t_n] = \mathrm{TP}[t_n] \times \mathrm{PF}[t_n]$. The $\mathrm{TP}[t_n]$ are measured from $n = 1, \ldots, N$ blood samples taken at time points t_n during the PET scan. When metabolite correction is used, $\mathrm{PF}[t_n]$ is estimated by interpolating a fitted metabolism function to $\mathrm{PF}[t_m]$, calculated after performing a high-performance liquid chromatography assay on $m = 1, \ldots, M$ blood samples, typically $M \ll N$. Indeed, fewer samples are analyzed for metabolites since it is expensive and laborious, and since the radioligand is no longer detectable in later time points if rapidly metabolized. We note that for a small group of radioligands PF(t)$\sim$1 (e.g., [^{18}F]FDG), and metabolite correction is, therefore, not needed. However, this tends to be an exception and not the rule. The final continuous-time AIF curve $y(t)$ is estimated by fitting an input function model to the measured samples $y[t_m]$.

The continuous $\mathrm{PF}(t)$ function is estimated by fitting $\mathrm{PF}[t_m]$ with a damped biexponential function as

$$\mathrm{PF}(t) = t^{\alpha}(C_1 e^{-\lambda_1 t} + C_2 e^{-\lambda_{\mathrm{cal}} t}) \tag{1}$$

where λ_{cal} is a calculated time constant equal to $\lambda_{\mathrm{cal}} = \lambda_{\mathrm{CER}} - \lambda_{\mathrm{TP}}$, using the terminal rate of washout of cerebellar activity λ_{CER} and the smallest elimination rate constant of the total

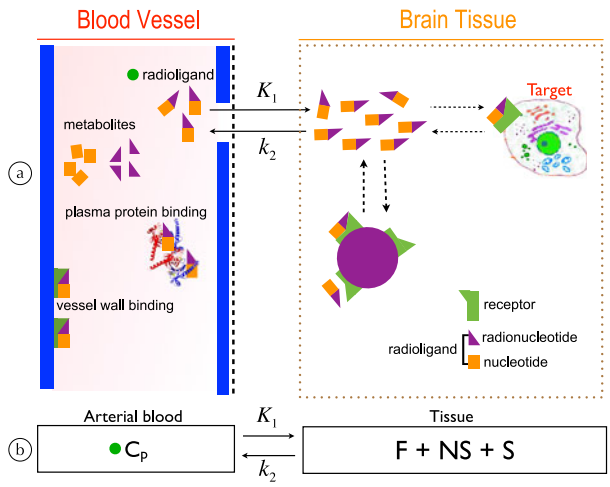

Fig. 1. Radioligand transfer between blood and brain tissue. (a) Radioligands are injected into the blood, diffuse into the brain, and bind to specific receptors at the brain tissue target site. Availability of radioligand in the blood plasma and tissue is limited due to metabolism, plasma protein and blood vessel wall binding, and nonspecific binding in the brain. (b) One-tissue compartment (1TC) model representation of the radioligand transfer illustrated in the upper panel. C_p is the freely available radioligand concentration in the arterial plasma, K_1 is the transfer rate from the arterial plasma to the tissue, k_2 is the transfer rate from the tissue back to the plasma. BBB—blood brain barrier.

plasma λ_{TP} [2]. The discrete-time AIF curve $y[t_n]$ was calculated and fitted with the following eight-parameter input function model

$$C_P(t|\theta^{\mathrm{IF}}) = \begin{cases} \alpha t & t < t_p \\ A_1 e^{-\lambda_1 t} + A_2 e^{-\lambda_2 t} + A_3 e^{-\lambda_3 t} & t \geq t_p \end{cases} \quad (2)$$

where $C_P(t|\theta^{\mathrm{IF}})$ is the AIF in continuous time, θ^{IF} parameters related to the input function model including the time of the peak of the input function t_P, the slope α, and the scale A_l and rate constants λ_l of the three-exponential function ($l = 1, 2, 3$), adjusted during the fit.

F. Time Activity Curves Modeling

For the [^{11}C]DASB radioligand, the transfer of radioligand from the vascular compartment into the brain tissues can be represented by a one-tissue compartment (1TC) model [29], as shown in Fig. 1. In this model, K_1 is the transfer rate of the radioligand from the arterial plasma to the tissue, where free, nonspecific, and specific binding are aggregated into a single compartment, k_2 is the transfer rate constant from the tissue back to the plasma. Mathematically, the regional TAC is encoded as a concentration function f of the radioligand in the tissue that can be formulated as a convolution product between the AIF, modeled with the parametric input function model C_p, and the tissue impulse response function $K_1 e^{-k_2 t}$ as

$$f(t, \theta^{\mathrm{IF}}, K_1, k_2) = K_1 e^{-k_2 t} \otimes C_P(t|\theta^{\mathrm{IF}}). \quad (3)$$

After collecting blood samples, θ^{IF} is first estimated by nonlinear least squares fitting of a continuous model of (2) to the measured metabolite-corrected arterial data $y[t_n]$. The resulting estimate $\hat{\theta}^{\mathrm{IF}}$ is substituted into (3). The rate constants are then estimated using iterative weighted nonlinear least squares minimization of the following function:

$$\sum_{j=1}^{J} w_j [Y_j - f(t_j|\theta^{\mathrm{IF}}, K_1, k_2)]^2 \quad (4)$$

where Y_j is the measured TAC from a brain region at points $j = 1, \ldots, J$ specified at time t_j, and w_j are weights here set to the frame duration of each time point.

G. Simultaneous Estimation (SIME)

The SIME approach simultaneously estimates the TAC parameters from multiple regions r, which are fitted at the same time. The parameters describing the IDIF are estimated by minimizing the following combined objective function:

$$\phi(t, \theta^{\mathrm{IF}}, \psi_r, \ldots, \psi_R) = \sum_{r=1}^{R} \sum_{j=1}^{J} w_j [Y_{rj} - f(t_j|\theta^{\mathrm{IF}}, \psi_r)]^2 + [y[t_{\mathrm{opt}}] - C_P(t_{\mathrm{opt}}|\theta^{IF})]^2 \quad (5)$$

where $y[t_{\mathrm{opt}}]$ is the metabolite-corrected radioligand concentration in the plasma measured at the predetermined optimum sampling time t_{opt}, $C_P(t_{\mathrm{opt}}\theta^{\mathrm{IF}})$ is the AIF model evaluated using the estimated parameters θ^{IF} at time t_{opt}, ψ_r is the vector of TAC parameters for the region r, $\psi_r = (K_{r1}, k_{r2})$, and Y_{rj} is the TAC measured from region r at time t_j. Minimization of this cost function is done with simulated annealing, a robust optimization technique for finding the global optimum [30].

H. Pharmacokinetic (PK) AIF Model

General characteristics of an AIF curve (see Fig. 3) include a bolus or short infusion phase followed by a postinfusion phase. During the infusion phase, the radioligand concentration increases until it peaks generally when infusion stops. The input function model of (2) has been utilized within SIME and previously applied to several radioligands [15]. This model assumes a linear rise from time zero to the peak at $t = t_p$ during the infusion phase and a decrease modeled by the sum of three exponentials during the postinfusion phase. As graphically shown in Fig. 2(a), after infusion starts at $t = 0$ the radioligand accumulates only in the central compartment for the infusion duration T. Then, immediately after infusion ceases, the distribution into other compartments in the body, and elimination phases begin.

Following this model, it is clear that if the infusion rate k_0 is constant, there will be a linear increase in the radioligand concentration in the central compartment, until infusion stops and the radioligand is distributed and eliminated. If a small volume of drug were injected, almost instantaneously (e.g., a vaccine injection) the model in Fig. 2(a) would be reasonable. In reality, however, the radioligand is usually diluted into a volume of several milliliter of saline or water and then infused manually, or with an infusion pump over a duration of ~10–60 s. In this case, infusion and elimination phases occur simultaneously and cannot be segregated. The infusion phase is nonlinear and typically begins with a delay relative to the PET acquisition due to

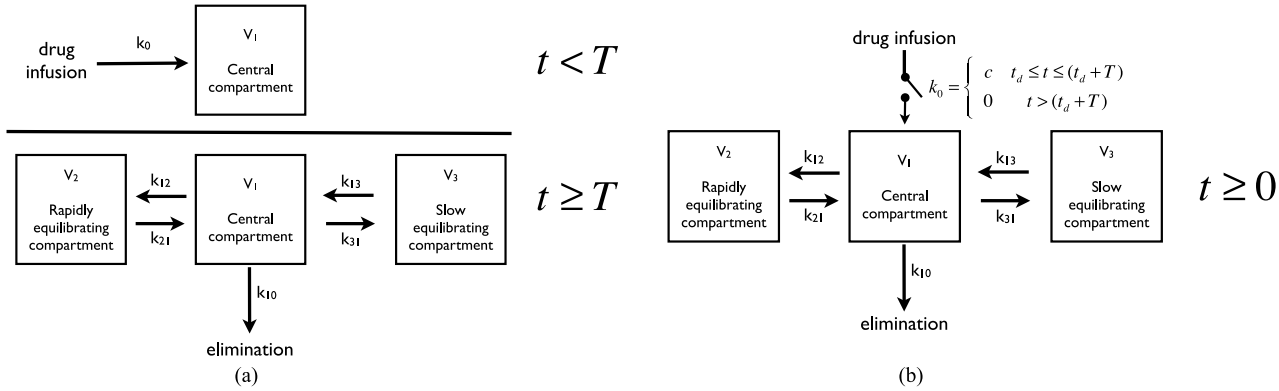

Fig. 2. Compartmental representation of the AIF models from which equations are derived. (left) Simple AIF model of (2), where the radioligand is infused into a virtual "central compartment" for the duration of time T at a rate k_0. Once infusion stops, the radioligand diffuses into other compartments and undergoes elimination. The rates of transfer between compartments are given by the k's (rate constants), V_l are volumes of each compartment $l = 1, \ldots, 3$. (right) The compartment PK AIF model of (6). The PET scan acquisition starts at $t = 0$, and after a delay t_d the radioligand infusion begins. As infusion is occurring, the radioligand is simultaneously accumulated in the central compartment, distributed to other compartments, and eliminated from the body.

blood travel time from the brain to the blood measurement site in the arm.

A more realistic representation of this system is described in Fig. 2(b), with a compartmental model, a delayed shunt-based infusion mechanism, and all compartments and data collection active at $t > 0$. After a delay time t_d, infusion begins and proceeds at a constant rate c. As the radioligand is infused, it simultaneously distributes into other compartments and is eliminated from the body through multiple pathways at a total rate k_{10}. After the infusion duration T, the shunt is closed, the infusion stops, while the distribution and elimination phases continue. This model has been described previously in the PK literature and is known as a three-compartment PK model of the drug plasma concentration [31], for which a combined infusion and postinfusion equation is readily derived using Laplace transforms and given by

$$C_p^{\mathrm{PK}}(t|\theta^{\mathrm{PK}}) = \begin{cases} \sum_{l=1}^{3} B_l \left(e^{-\lambda_l (t-t_d)} - 1\right), & t < T \\ \sum_{l=1}^{3} B_l \left(e^{-\lambda_l T} - 1\right) e^{-\lambda_l (t-t_d)}, & t \geq T \end{cases} \quad (6)$$

where $C_p^{\mathrm{PK}}(t|\theta^{\mathrm{PK}})$ is the concentration of parent radioligand in the plasma in continuous time, including some parameters θ^{PK} related to the PK input function model (e.g., t_d, B_l, λ_l, T). B_l and λ_l are, respectively, the scaling and rate constants for the lth compartment of the input function, and t_d and T are, respectively, the delay and infusion duration.

We note that infusion and postinfusion components share the same parameters, which allows the model to take advantage of data acquired during infusion to describe the data acquired postinfusion. Examples of the application of the simple and the PK-based AIF models from (2) and (6) are shown in Fig. 3. A variation of this model has been previously utilized in PET but did not include a delay term, and was only described by a set of ordinary differential equations that were fit to the data using Levenberg–Marquardt optimizer [32]. The explicit parametric formulation of the PK model provided in (6) enables this model to be utilized with the SIME cost function.

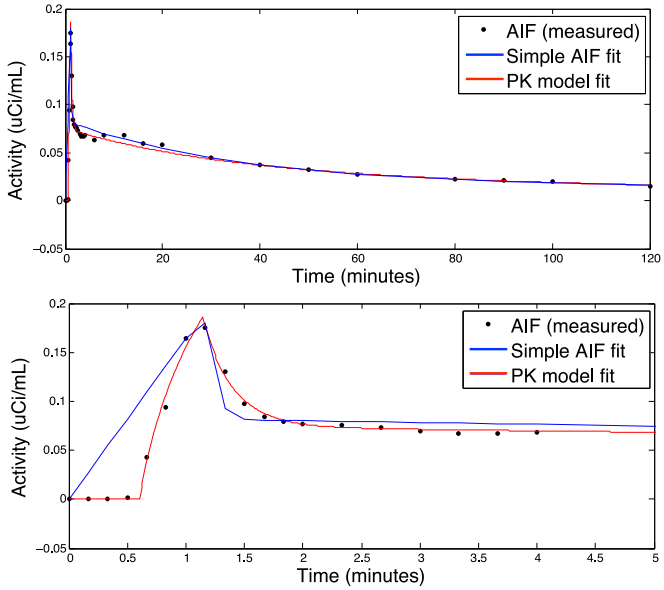

Fig. 3. Comparison of AIF model fits: Measured AIF (black dots), AIF fitted with nonlinear least squares using a simple model of (2) and currently used by SIME (blue line), and proposed PK AIF model of (6) (red line).

I. Noninvasive SIME (nSIME) Objective Function

SIME requires a constraint to ensure identifiability of the model. Currently, this constraint is based on one measured blood sample taken at an empirically determined optimum sampling time. For [^{11}C]DASB, this sample is taken at $t_{\mathrm{opt}} = 50$ min after injection. It is used to measure $\mathrm{TP}[t_{\mathrm{opt}} = 50]$ and $\mathrm{PF}[t_{\mathrm{opt}} = 50]$, allowing us to sample the AIF at that optimal time, $y[t_{\mathrm{opt}} = 50]$, which for clarity we will refer to hereinafter as AIF50.

Population PK studies show that it is possible to make individualized predictions for clearance and area under the curve (AUC) for many pharmaceutical compounds [18]. Such prediction is typically performed using mixed effects modeling to identify significant covariates among various indicative variables derived from weight, GFR, etc. In this study, we propose to investigate the development of a predictive model for AIF50 that uses noninvasive patient information. The predicted blood

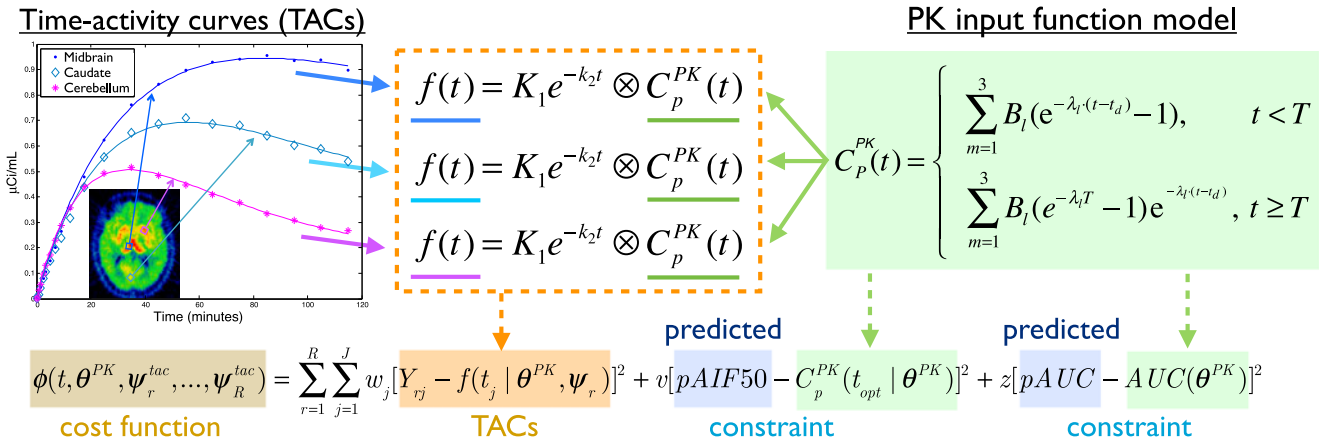

Fig. 4. Overview of the nSIME approach showing elements of the cost function that are minimized using simulated annealing. Shape and scale of the input function are inferred from simultaneous fitting of TACs constrained by AIF50 and AUC predictions.

sample value pAIF50 then replaces AIF50, thus making SIME completely blood free. To provide additional robustness, we also predict the PK variable AUC, which is a more stable measure than AIF50 as it is calculated from multiple time point samples. We then incorporate the predicted value pAUC as an additional constraint within SIME. The combined objective function with predicted constraints becomes

$$\phi(t,\theta^{\mathrm{PK}},\psi_r^{\mathrm{tac}},\ldots,\psi_R^{\mathrm{tac}}) = \sum_{r=1}^{R}\sum_{j=1}^{J} w_j\,[Y_{rj} - f(t_j|\theta^{\mathrm{PK}},\psi_r)]^2 + v[\mathrm{pAIF50} - C_p^{\mathrm{PK}}(t_{\mathrm{opt}}|\theta^{\mathrm{PK}})]^2 + z[\mathrm{pAUC} - \mathrm{AUC}(\theta^{\mathrm{PK}})]^2 \quad (7)$$

where pAIF50 and pAUC are the predicted AIF50 and AUC constraints, v and z are empirical weights, and the function AUC is given by

$$\mathrm{AUC}(\theta^{\mathrm{PK}}) = \int_0^{\infty} C_p^{\mathrm{PK}}(t|\theta^{\mathrm{PK}})dt. \quad (8)$$

Following [15], [33], the empirical weight for the AIF50 constraint was set to $v = 100$ to ensure that the estimated input function passes through pAIF50. The weight for the AUC constraint was empirically set to $z = 5$ such that the two constraint error terms have similar magnitude and contribute equally to the cost function. An overview of the nSIME approach is shown in Fig. 4.

J. Selection of Noninvasive Patient Variables

The noninvasive patient information available for the predictive model combines EHR, PET image-derived information, demographics, and derived variables, amounting to a total of 100 potential predictors listed in Table II. Of the PET-derived predictors, the TAC sum refers to the cumulated sum between 50 min and the end of the scan and is calculated for each of the seven preselected manual ROIs. Similarly, $\mathrm{TPsum} = \int_{50}^{\infty} \mathrm{TP}(t)dt$ corresponding to the integration of TP values from 50 min after the injection to the end of the scan. We also include λ_{cal} from (1) and use it to estimate the portion of ID eliminated from the body after 50 min due to first order clearance, defined as $e\mathrm{ID50} = \mathrm{ID}^{(-\lambda_{\mathrm{cal}}50)}$. Although the aforesaid are technically invasive measures, in the future TP and λ_{cal} may be replaced by measuring whole blood radioligand concentration with IDIF methods (see Section I), or a PET wrist scanner [34], and by scaling this measure using a whole blood to plasma conversion factor (see Section IV for a discussion).

TABLE II
INITIAL SET OF 100 VARIABLES CONSIDERED AS POTENTIAL PREDICTORS

Initial Predictors (100)			
Chemistry (21)	**Thyroid (5)**	**Urinalysis (3)**	**Demographics (4)**
A/G Ratio	T3 Uptake	Specific Grav Urine	Weight
Albumin	TSH	Urobilinogen	Height
Alk Phos	Thyroxine Free	pH	Age
ALT(SGPT)	Thyroxine Total		Sex
AST(SGOT)	Triiodothyronine	**Derived (16)**	
BUN		BMI	**Vitals (24)**
Calcium	**Hematology (14)**	BSA	HR
Chloride	WBC	LBMI	BPs, BPd
Cholesterol	RBC	eTBV	MAP
CO2	Hemoglobin	eTPV	PP
Creatinine	Hematocrit	eGFR	eCO
Globulin	MCV	eGFRBSA	x2 (pre, post)
Glucose	MCH	eGFR5	x2 (closest, avg)
LDH	MCHC	eGFR5BSA	
Phosphorus	RDW	eRMR	**PET (13)**
Potassium	Platelets	Osmolarity Gap	TAC sum (x7)
Sodium	Neut Absolute	rCalcium	TPsum
T. Bilirubin	Lymph Absolute	Blood viscosity	ID
Total Protein	Mono Absolute	Anion gap	eID50, λcal
Triglyceride	Eosin Absolute	BUN:Crt ratio	Injected Mass
Uric Acid	Baso Absolute	Plasma osmolarity	Specific Activity

The following multistage approach is proposed to screen for variables that may be useful in predicting AIF50 and AUC. First, since TACs are highly correlated between regions, we only keep as a potential predictor the TAC sum with the highest correlation with AIF50 and AUC. It was found to be the cerebellum TAC sum (noted CERsum).

Next, the 94 remaining predictors (after removing the six other TAC sums) are screened based on their correlations with the measured AIF50 and retained if $R^2 > 0.1$. From the 94 predictors we also generate a series of normalized ID variables by dividing each predictor variable into ID, since interactions between dose and physiology are expected for some variables.

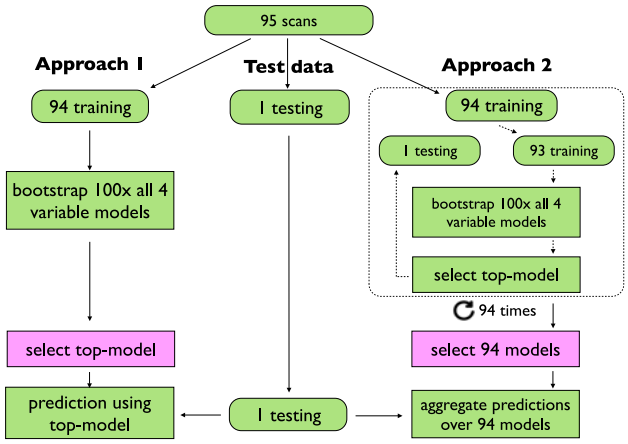

Fig. 5. Machine learning approaches: Approach 1 = Top-model, Approach 2 = aggregate model.

The normalized ID variable is retained for further analysis if the R^2 correlating it with AIF50 is greater than the R^2 correlating it with ID. Finally, again considering the 94 predictors, we conducted a search of two-variable interaction terms. A total of 4371 (choose two out of 94) multivariate regression models are evaluated, each consisting of two predictors with and without interaction terms. The interaction term is retained if the R^2 of the model with the interaction term is both greater than 0.1, and is greater than the R^2 of the model without the interaction term, and the p-value of the interaction term is less than 0.05. The entire screening procedure is repeated for AUC. Sex (binary variable) is only included during the interaction term screening step. To mitigate effects of multicollinearity and different value ranges among the predictors, all variables (except Sex) are normalized into Z-scores (zero mean and unitary standard deviation). A total of 56 predictors were selected for AIF50 and 52 predictors for AUC.

K. SIME Constraints Prediction

We developed two approaches that combine the simplicity and interpretability of linear regression (LR) with robustness to outliers and noise of random forests and boosting. The first approach consists of a bootstrapped best-model selection procedure, and the second approach is designed as a new bootstrapped model aggregation method. For clarity, a flow diagram for both approaches is shown in Fig. 5.

Bootstrapped top-model selection: First, a leave-one-out procedure is employed where one of the scans is left out for testing and the rest of the scans ($N = 94$) are used for training. Second, for the training set, all possible four variable LR models are assessed leading to 367,290 (choose four out of 56) for AIF50 and 270,725 (choose four out of 52) for AUC. Third, bootstrapped average R^2 correlations are calculated from training each model 100 times using randomly drawn samples with replacement from the training data. Fourth, the model with the highest R^2 is applied to the test data. The procedure is repeated 95 times, once for each observation.

Bootstrapped aggregate model selection: This procedure utilizes two nested leave-one-out loops to find a set of models that are aggregated and whose predictions are averaged. First, the dataset of 95 observations is split into test-level1 and training-level1 ($N = 94$). Second, the training set training-level1 is split again into test-level2 and training-level2 ($N = 93$). Third, for level 2 of the training set, all possible four variable LR models are assessed: 367,290 (choose four out of 56) for AIF50 and 270,725 (choose four out of 52) for AUC. Fourth, bootstrapped average R^2 correlations are calculated from training each model 100 times using randomly drawn samples with replacement from the training data. Fifth, the model with the "best" (minimal error) prediction for the test set test-level2 is selected. Repeating this procedure for all 94 training-level1 observations, we generate 94 optimal LR predictive models. Finally, these 94 models are aggregated (averaged) to predict the test-level1 observation.

The advantage of this approach is threefold: 1) all possible four variable LR models are tested; 2) each training data point contributes only with a weight of 1/94 to the overall prediction, thereby reducing impact of outlier observations without removing points from the training data; 3) since training points span a large range of values, selecting the LR predictive model with the "minimal error" for each point yields a set of models optimal for narrow ranges of values, improving the chances that at least some of the models will provide reasonable predictions for any test point.

L. Performance Evaluation

Predicted pAIF50 and pAUC values obtained using the two proposed approaches are incorporated as constraints into the nSIME objective function of (7). Either the measured or nSIME derived input function can be substituted into (4) to estimate kinetic rate constants and to derive the outcome measures of interest (V_T, BP_P and $\mathrm{BP}_{\mathrm{ND}}$), as described in Section I. For each region and scan, the aforesaid measures were estimated using kinetic modeling with the measured AIF (from full arterial sampling) and nSIME. Agreement between the two approaches was assessed via correlation and regression analysis on the estimates, using the nSIME-derived AIF as a dependent variable and the measured AIF as the independent variable. All analyses were done using MATLAB 2012a (The Mathworks, Inc.) on a 12 CPU Intel Xeon E5–2690 2.90 GHz and 128-GB RAM Linux server. For each PET scan, training of the top-model and aggregate-model took ~45 and 430 min, respectively, using all CPUs. Testing time was ~1 min. Computational time for nSIME was ~30 min on a single CPU.

III. Results

A. Prediction of AIF50 and AUC

Predictions from the two machine learning approaches are shown as Bland–Altman plots in Fig. 6 for AIF50 and AUC variables. The top-model and aggregate model predictions yielded, respectively, a correlation between predicted and measured values of 0.769 and 0.824 for AIF50, and 0.727 and 0.790 for AUC. Therefore, both prediction models returned high correlation values ($r > 0.72$) for the two predicted values and the aggregate model yielded higher correlations for both variables.

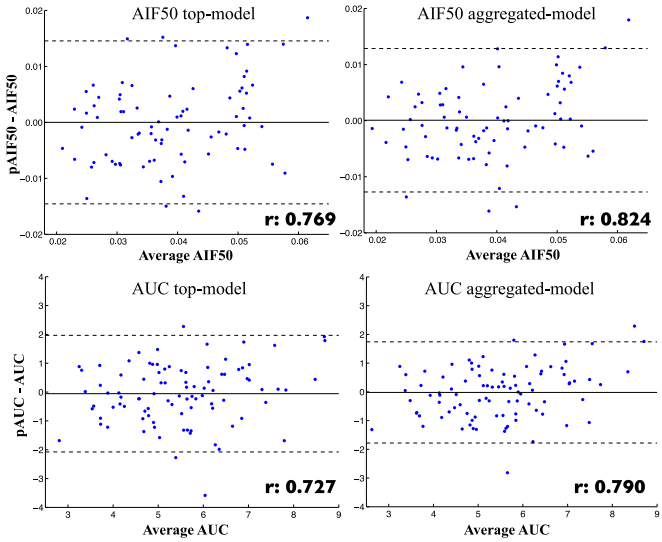

Fig. 6. Bland–Altman plots comparing leave-one-out predicted constraints (pAIF50, pAUC) to measured values (AIF50, AUC). Mean (solid) and mean +/− 1.96∗STD (dashed) lines, and Pearson's correlation (*r*) between predicted and measured constraint are shown for reference.

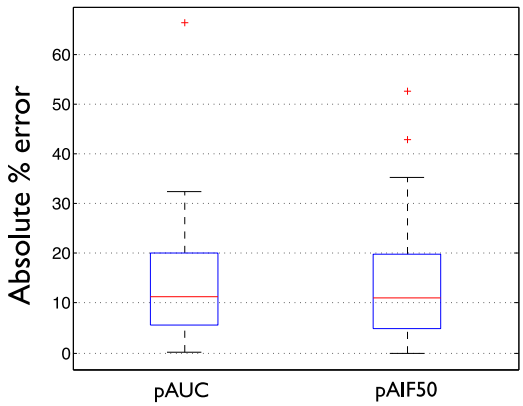

Fig. 7. Absolute% error for predicted variables pAUC and pAIF50 from the aggregate model. Boxplots show first and third quartiles as bottom and top box boundaries, and median value as the red line. Whiskers indicate 1.5 times lower and upper interquartile range with red (+) indicates outliers.

There is no evidence of bias (mean difference is close to zero) in the estimated variables. Even though few points lie outside the 95% interval, variance does not appear to increase with magnitude. Considering the aggregate model, prediction errors are plotted as boxplots in Fig. 7. Absolute percent error for pAUC and pAIF50, for most scans, were within the first–third quartile intervals: [5.5–20.2%] and [4.8–19.9%], respectively. One scan had a pAIF50 error $>$ 60% and two scans had pAUC errors $>$40%.

To assess the relative importance of predictors, we calculated the frequency of occurrence of each predictor as a variable in the top-model across all 95 top models. These frequencies are reported in Table III. For pAIF50, the top three most frequent predictor variables were CERsum (34.7%), TPsum (22.9%), and the interaction term HRpost∗TPsum (13.9%). For pAUC, the top three most frequent predictor variables were

TABLE III
FREQUENCY OF PREDICTOR VARIABLE APPEARANCE IN THE BOOTSTRAPPED MODELS SELECTED BY THE TOP-MODEL PREDICTION APPROACH

pAIF50 top-model		pAUC top-model	
Variable	Frequency	Variable	Frequency
CERsum	34.7%	TPsum	26.8%
TPsum	22.9%	CERsum	24.7%
HR_post∗TPsum	13.9%	BSA∗PP_post	18.4%
BPd_pre∗Eosin	13.7%	eGFR5BSA∗PP_post	17.9%
HR_avg∗CERsum	12.9%	eTBV∗Potassium	14.5%
ID/HR_pre	4.2%	eID50	12.6%
BPd_closest∗Eosin	3.4%	CERsum∗eID50	12.4%
TPsum∗Chloride	2.4%	eRMR∗Potassium	5.8%
ID/HR_closest	1.6%	Height	2.1%
Weight∗HR_post	1.3%	LBMI∗TotalProtein	2.1%
ID/eRMR	1.1%	TPsum∗PlasmaOsm	1.6%
HR_post∗CERsum	0.8%	TPsum∗HR_avg	1.3%
ID/HR_avg	0.5%	TPsum∗Sodium	1.3%
ID/BPd_post	0.3%	Height∗Urobilinogen	1.3%
ID/HR_post	0.3%	TPsum∗osmGAP	1.3%

Normalized ID variables are indicated as "ID/variable," while ∗ represents an interaction term between two predictors (multiplication of values). Some variables were measured before (_pre) or after (_post) the PET scan, the average (_avg) of before/after the PET scan, or closest to the PET scan time.

TPsum (26.8%), CERsum (24.7%), and the interaction term BSA∗PPpost (18.4%).

Overall, for pAIF50, 35.5% and 17.0% of all selected predictor variables contained, respectively a HR- or BP-based term. In contrast, for AUC, 0.3% and 33.1% of all selected predictor variables contained, respectively, a HR- and BP-based term.

B. AIF Estimations

Measured and nSIME-derived input functions are shown for representative cases in Fig. 8. To illustrate the separate effects that errors in pAUC and pAIF50 impart on the input function estimation, scans were selected with two different error levels for (pAIF50/pAUC): [see Fig. 8(a)] low/low; [see Fig. 8(b)] low/high; [see Fig. 8(c)] high/low and [see Fig. 8(d)] high/high. It appears that AIF50 primarily impacts the height and shape of the tail portion of the curve (beyond 40+ min), while AUC controls the offset of the entire curve. The tail part of the curve is best recovered when pAIF50 error is low while the initial part of the curve is heavily influenced by pAUC. When pAUC error is high, the initial part is over- or underestimated, driven by the sign and magnitude of the pAUC error. In general, it is difficult to disentangle the influence of pAUC and pAIF50 since the constraints are working together and in conjunction with the dynamic PET imaging data to recover the shape of the AIF curve. So it is not clear which measure is driving the objective function for a given scan. We illustrate on Fig. 9 two cases where pAUC and pAIF50 have large errors of opposite signs, and therefore the two constraints compensate for one another. In Fig. 9(a), pAUC error is −8.9% and pAIF50 error is +9.0%, while in Fig. 9(b) pAIF50 error is +9.2% while pAIF50 error is −11.3%. In both cases, nSIME was able to recover the input function quite well, especially the tail part beyond 30 + min. This suggests that the constraints are counteracting one another

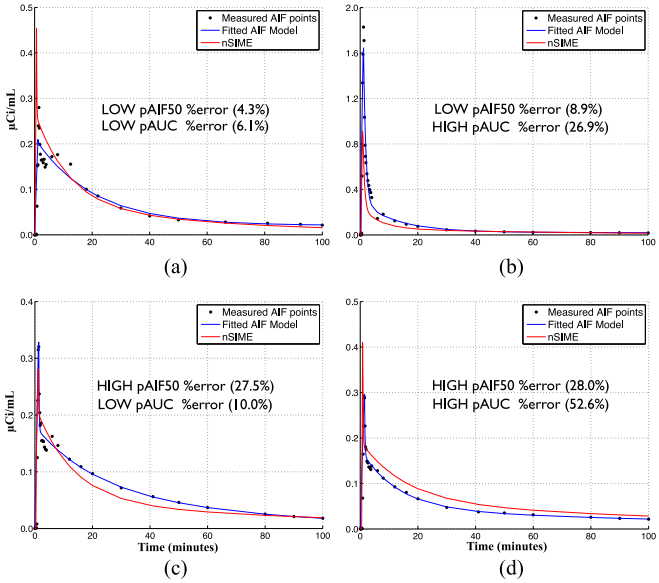

Fig. 8. Comparison of AIF curves derived from blood measures (black dots) and fitted with the model (2) (blue line) and nSIME with aggregate model predicted constraints (red line). Four representative cases are illustrated, with low/high pAIF50 (a, c) or low/high *p*AUC (b, d) percent errors.

and ultimately reduce the impact of their individual errors. For such cases having multiple constraints appears to yield benefits for AIF recovery.

C. Outcome Measures

Kinetic modeling outcome measures V_T, $\mathrm{BP_{ND}}$, and BP_P were computed using measured AIF and nSIME-derived input functions. Bland–Altman plots and Pearson's correlation coefficients for these outcome measures for seven brain regions are shown in Fig. 10. A low bias (mean difference close to zero) is visible for all outcome measures. A tendency toward higher variance with increasing values is observed for all variables, but slightly less pronounced for V_{T}. These plots also enabled us to identify two problematic PET scans, noted #1 and #2, which generated extreme outlier points, far outside the 95% limits of agreement for all three measures. The pAIF50 and pAUC errors are -6.1% and $+25.4\%$ for scan #1, and $+74.8\%$ and $+37.9\%$ for scan #2, respectively. Scan #1 had the lowest AIF50 value and the highest radioligand clearance rate of any scan in our sample. Interestingly, scan #2 had relatively small constraint prediction errors but very poor nSIME PK model and TAC parameter estimates. This is likely due to an unusual large secondary peak present in the measured AIF. This secondary peak could be due to radioligand partial injection into tissue followed by slow diffusion back into the arterial supply (prolonged bleeding was noted for this subject), error in metabolite modeling, or possibly a true radioligand recirculation component that is not taken account by our PK model.

nSIME estimations returned high correlation values across all brain regions, the lowest being for V_{T} with $r = 0.877$. Regional correlations were always lower than global brain correlation values except in the temporal lobe. Regional correlation values vary a lot between regions, but always follow the following ranking:

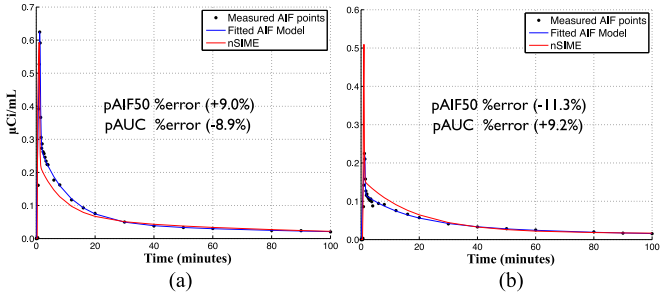

Fig. 9. Behavior of nSIME derived AIF input functions when errors of pAIF50 and pAUC are of opposite signs. In (a), pAUC error is negative and pAIF50 error is positive while in (b), pAUC error is positive and pAIF50 error is negative. In both cases, the recovered curve matches well the AIF tail portion beyond the 30 min time point.

$r_{\mathrm{BP_{ND}}} > r_{\mathrm{BP_P}} > r_{\mathrm{V_T}}$. The highest regional correlation value was found for $\mathrm{BP_{ND}}$ in the temporal lobe with $r = 0.970$, which beats the global brain correlation value for the same measure.

IV. Discussion

We have introduced the concept of nSIME, as a new SIME framework to enable full noninvasive quantitative PET imaging. This framework replaces blood-based radioligand measures by a robust PK input function model and multiple noninvasive constraints based on machine learning on EHR data. Our results on a large database of [^{11}C]DASB brain PET images showed that nSIME predictions of volume of distribution and binding potentials were highly correlated with estimates based on full arterial blood sampling.

In this evaluation, we also discovered specific covariates that appear to be related to [^{11}C]DASB metabolism and clearance from the body, which may be useful for understanding and interpreting the radioligand kinetics. CERsum was frequently included in the predictive models, which is interesting because the cerebellum is commonly used as a reference region for [^{11}C]DASB [29].

Another interesting result is that HR and BP appear more important for AIF50 prediction, while body size related terms (e.g., BSA, eGFR, eTBV) appear more frequently selected for AUC predictive models. There are two plausable explanations for the association of HR and BP with [^{11}C]DASB metabolism. First, from a hemodynamic point of view, the higher HR and BP, the greater the cardiac output and thus blood flow. Indeed, it has been shown that radioligand uptake is alterated during anesthesia beause of reduced HR and BP, and thus blood flow [35]. Second, [^{11}C]DASB binds the serotonin transporters whose function is associated with cardiac repolarization intervals and HR variability [36], [37]. The relationship between body size terms and AUC is possibly more straightforward and can be inferred from Fig. 2(b). Body size impacts the volume of the compartments, plasma concentration of radioligand decreases when radioligand is diluted into a larger plasma volume.

Our results are particularly encouraging since EHR data are heterogeneous and some measures are quite crude. For example, the EHR data were gathered retrospectively and included measures that were acquired anywhere from hours (e.g., HR,

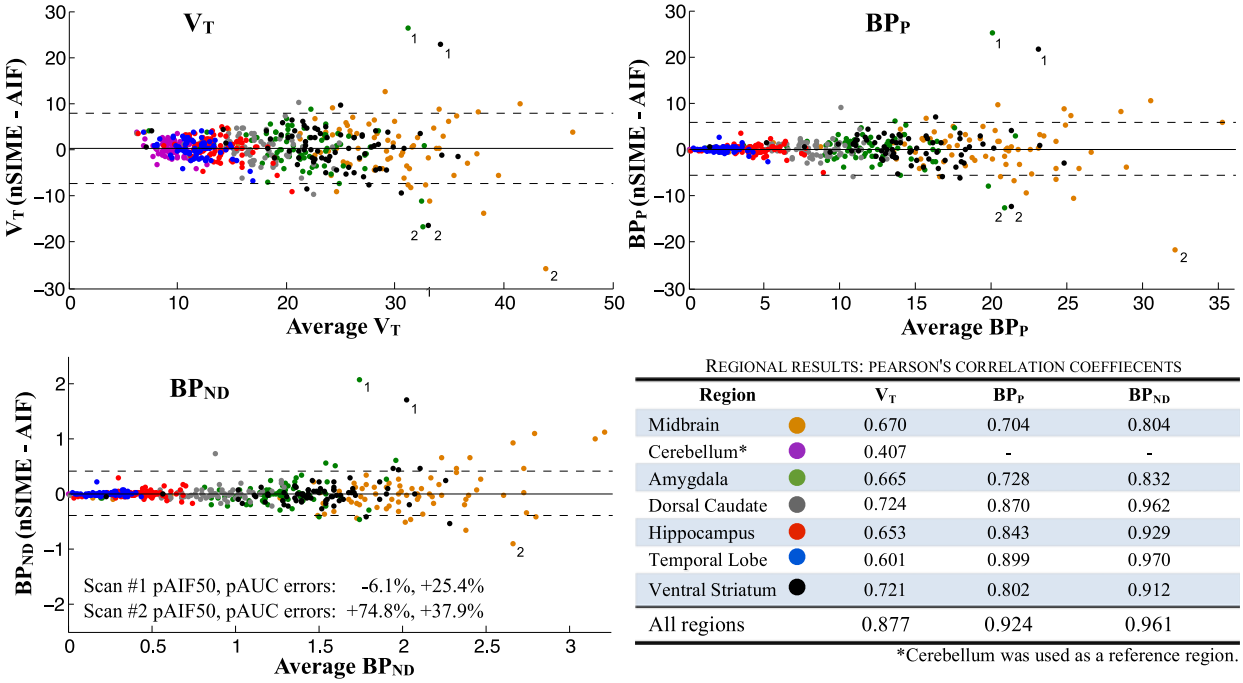

REGIONAL RESULTS: PEARSON'S CORRELATION COEFFIECENTS

Region	V_T	BP_P	BP_{ND}
Midbrain	0.670	0.704	0.804
Cerebellum*	0.407	-	-
Amygdala	0.665	0.728	0.832
Dorsal Caudate	0.724	0.870	0.962
Hippocampus	0.653	0.843	0.929
Temporal Lobe	0.601	0.899	0.970
Ventral Striatum	0.721	0.802	0.912
All regions	0.877	0.924	0.961

*Cerebellum was used as a reference region.

Fig. 10. Bland–Altman plots of estimated outcome variables V_T, BP_P, and $\mathrm{BP}_{\mathrm{ND}}$ derived using nSIME and the measured AIF for all regions and scans. Mean (black) and 95% limits of agreement (dashed) lines are included for reference. Extreme outlier points from two scans (scan #1 and scan #2) are labeled. Brain regions are specified in different colors as depicted within the inset table. The inset table shows Pearson's correlation coefficients for each individual brain region and across all brain regions, separately for each outcome measure. The binding potentials ($\mathrm{BP_P}$ and $\mathrm{BP_{ND}}$) are by definition zero for the reference region.

BP) to weeks (e.g., hematocrit, creatinine) from the PET scan time. Weight was measured up to months before the scan and HR was measured via manual radial pulse rate.

Two predictive models were proposed for AIF50 and AUC, and confirmed the possibility to recover the AIF of the [^{11}C]DASB radioligand without blood samples. Some outliers remain that might very well be due to erroneous EHR measures and/or errors in measured blood samples, to be confirmed with a quality-controlled prospective study.

There are still a few limitations that prevented us from achieving a fully noninvasive PET image quantification tool. First, among the most frequently selected predictors in our predictive models for AIF50 and AUC were TPsum and eID50 (based on λ_{cal}). Both variables are technically "invasive," but may eventually be supplemented with an IDIF after correcting for the whole blood to plasma partition. Developing IDIF-based TPsum and λ_{cal} measures is the subject of future work. Previous works have shown that the whole blood curve may be estimated from the PET signal from carotid arteries, by scaling using the maximum value for [^{18}F]FDG [38] or the average of four hottest pixels for [^{11}C]flumazenil [39]. A whole blood to plasma correction factor may then be derived in a similar manner to [40], based, for example, on hematocrit (e.g., [^{18}F]FTHA, [^{11}C]WAY) or on a population average function of the whole blood to plasma ratio (e.g., [^{11}C]HED, [^{11}C]MP4A). For [11C]DASB, the whole blood to plasma ratio changes over the course of the scan but begins to equilibrate after 50 min [41]. A population average function for the 50+ min portion could be used to convert the whole blood IDIF into a "plasmatic" IDIF, enabling TPsum and λ_{cal} to be calculated using only information from 50+ min of the IDIF. Also, given that [^{11}C]DASB is known to accumulate within red blood cells [41], it may be possible to predict the red blood cell concentration of [^{11}C]DASB using a combination of IDIF and the EHR (e.g., by using hematocrit and red blood cell count).

Second, confirmation of the reported prediction accuracy of our nSIME relies on the availability of a large training set of data consisting of PET images, EHR data and blood-based AIFs, from which to build and test a predictive model for the constraints. The number of scans needed for "optimal" training still needs to be investigated and likely varies from radioligand to radioligand. It is also plausible that the subject population may influence results.

Third, alternative noninvasive reference tissue approaches are available to estimate [^{11}C]DASB $\mathrm{BP_{ND}}$. A previous study with 209 [^{11}C]DASB scans reported good performance with either a simplified reference tissue method, ($r = 0.933$, slope $= 0.972$) or a multilinear reference tissue model approach ($r = 0.973$, slope $= 0.947$) [42]. With nSIME, albeit with fewer scans, our results for $\mathrm{BP_{ND}}$ yielded a slope that is closer to identity and correlation values that were between the two. This previous study noted poor performance with [^{11}C]DASB on the voxel analysis when comparing the multilinear reference tissue approach to graphical analysis with full arterial blood sampling ($r = 0.508$) [42]. Better performance of voxel analysis might be achieved with nSIME because it estimates an input function that could be used with graphical analysis. In general, we emphasize that reference tissue approaches are limited to estimating $\mathrm{BP_{ND}}$ only while our approach is not.

Fourth, the ability of nSIME to predict f_P and estimate BP_F was not explored in this study. However, a recent study by our group reported prediction of $f_{\mathrm{P}} * \mathrm{AIF50}$ for the radioligand [^{11}C]CUMI with a high correlation ($r > 0.9$), using only ID and BMI (or BSA) [43]. For our [^{11}C]DASB scans, all individual

predictors correlated poorly with f_P ($R^2 < 0.1$), and predictor correlations with $f_P * \text{AIF50}$ were consistently lower than for AIF50 alone (data not shown). We expect the ability of nSIME to predict f_P to vary by radioligand, depending on mechanism of radioligand binding to plasma proteins, and the quality and detail of the EHR record. Incorporating f_P prediction into nSIME, and validation across radioligands, is the subject of future work.

Despite these limitations, [^{11}C]DASB is one of the most challenging radioligands to analyze because it has metabolite kinetics affected by lung trapping [2] and undergoes significant metabolism [29]. Our approach does not require any assumptions with respect to these issues. Since we estimate the AIF directly, metabolite modeling is not needed and any level of metabolism can be handled implicitly. Thus, nSIME approach may be applied to any radioligand once a model for predicting constraints has been developed.

Acronym	Definition
ID	injected dose of the radioligand
IDIF	image derived input function
LBMI	lean body mass index
nSIME	noninvasive SIME (proposed approach)
pAIF50	predicted AIF50 using machine learning on EHR data
pAUC	predicted AUC using machine learning on EHR data
PF	parent fraction of unmetabolized radioligand measured in the plasma of a selection of blood samples
PP	estimated pulse pressure
PPKD	population pharmacokinetics and pharmacodynamics
ROI	region of interest
SIME	simultaneous estimation
TAC	time-activity curve
TP	total radioactivity concentration of the radioligand and metabolites in the plasma
TPsum	sum of the TP curve beyond 50+ min
V_T	volume of distribution
W	weight

V. Conclusion

We have designed an original big-data analytics tool toward a noninvasive nSIME quantitative method for PET imaging, by combining time-series PET images with EHR records. The application shows that we can exploit EHR data to transform PET screening into a simpler medical examination tool and also obtain new knowledge about the relationship between patient physiology and PET radioligand metabolism and clearance. The promising results highlight the potentials of big-data analytics for PET imaging. Development of public databases of previously unused ancillary records collected routinely with PET scans should be encouraged to pursue this transforming path.

Glossary of Technical Abbreviations

Acronym	Definition
λ_{cal}	slope of the TP curve beyond 50+ min
AIF	arterial input function measuring the metabolite corrected concentration of radioligand in the plasma
AIF50	the AIF value at 50 min after injection
AUC	the total area under the AIF curve
BMI	body mass index
BP	blood pressure
BPd	diastolic blood pressure
BP_F	binding potential (relative to plasma and f_P)
BP_{ND}	binding potential (relative to nondisplaceable compartment)
BP_P	binding potential (relative to plasma)
BPs	systolic blood pressure
BSA	body surface area
CERsum	sum of the cerebellum TAC beyond 50+ min
eGFR	estimated glomerular filtration rate
eGFR5	eGFR formula that includes nitrogen and albumin
eGFR5BSA	eGFR5 adjusted to each individual's BSA
EHR	electronic health record
eID50	estimated amount of injected dose eliminated from the body after 50 min
eTBV	estimated total blood volume
f_P	free fraction of the radioligand in the plasma
H	height
Hct	hematocrit
HR	heart rate

References

[1] R. B. Innis, V. J. Cunningham, J. Delforge, M. Fujita, A. Gjedde, R. N. Gunn, J. Holden, S. Houle, S. C. Huang, M. Ichise, H. Iida, H. Ito, Y. Kimura, R. A. Koeppe, G. M. Knudsen, J. Knuuti, A. A. Lammertsma, M. Laruelle, J. Logan, R. P. Maguire, M. A. Mintun, E. D. Morris, R. Parsey, J. C. Price, M. Slifstein, V. Sossi, T. Suhara, J. R. Votaw, D. F. Wong, and R. E. Carson, "Consensus nomenclature for *in vivo* imaging of reversibly binding radioligands," *J. Cereb. Blood Flow Metab.*, vol. 27, pp. 1533–1539, Sep. 2007.

[2] R. V. Parsey, A. Ojha, R. T. Ogden, K. Erlandsson, D. Kumar, M. Landgrebe, R. Van Heertum, and J. J. Mann, "Metabolite considerations in the *in vivo* quantification of serotonin transporters using 11C-DASB and PET in humans," *J. Nucl. Med.*, vol. 47, pp. 1796–802, Nov. 2006.

[3] P. Zanotti-Fregonara, K. Chen, J. S. Liow, M. Fujita, and R. B. Innis, "Image-derived input function for brain PET studies: Many challenges and few opportunities," *J. Cereb. Blood Flow Metab.*, vol. 31, pp. 1986–1998, Oct. 2011.

[4] R. N. Gunn, S. R. Gunn, and V. J. Cunningham, "Positron emission tomography compartmental models," *J. Cereb. Blood Flow Metab.*, vol. 21, pp. 635–652, Jun. 2001.

[5] M. A. Kropholler, R. Boellaard, A. Schuitemaker, H. Folkersma, B. N. van Berckel, and A. A. Lammertsma, "Evaluation of reference tissue models for the analysis of [11C](R)-PK11195 studies," *J. Cereb. Blood Flow Metab.*, vol. 26, pp. 1431–1441, Nov. 2006.

[6] S. M. Ametamey, V. Treyer, J. Streffer, M. T. Wyss, M. Schmidt, M. Blagoev, S. Hintermann, Y. Auberson, F. Gasparini, U. C. Fischer, and A. Buck, "Human PET studies of metabotropic glutamate receptor subtype 5 with 11C-ABP688," *J. Nucl. Med.*, vol. 48, pp. 247–252, Feb. 2007.

[7] T. Tsuchida, N. Sadato, Y. Yonekura, S. Nakamura, N. Takahashi, K. Sugimoto, A. Waki, K. Yamamoto, N. Hayashi, and Y. Ishii, "Noninvasive measurement of cerebral metabolic rate of glucose using standardized input function," *J. Nucl. Med.*, vol. 40, pp. 1441–1445, Sep. 1999.

[8] M. Bentourkia, "Kinetic modeling of PET-FDG in the brain without blood sampling," *Comput. Med. Imaging Graph*, vol. 30, pp. 447–451, Dec. 2006.

[9] B. J. Lopresti, W. E. Klunk, C. A. Mathis, J. A. Hoge, S. K. Ziolko, X. Lu, C. C. Meltzer, K. Schimmel, N. D. Tsopelas, S. T. DeKosky, and J. C. Price, "Simplified quantification of Pittsburgh compound B amyloid imaging PET studies: A comparative analysis," *J. Nucl. Med.*, vol. 46, pp. 1959–1972, Dec. 2005.

[10] K. Chen, D. Bandy, E. Reiman, S.-C. Huang, M. Lawson, D. Feng, L.-s. Yun, and A. Palant, "Noninvasive quantification of the cerebral metabolic rate for glucose using positron emission tomography, 18F-Fluoro-2-Deoxyglucose, the Patlak method, and an image-derived input function," *J. Cereb. Blood Flow Metab.*, vol. 18, pp. 716–723, 1998.

[11] M. Schain, S. Benjaminsson, K. Varnas, A. Forsberg, C. Halldin, A. Lansner, L. Farde, and A. Varrone, "Arterial input function derived from pairwise correlations between PET-image voxels," *J. Cereb. Blood Flow Metab.*, vol. 33, pp. 1058–1065, Jul. 2013.

[12] E. K. Fung, B. Planeta-Wilson, T. Mulnix, and R. E. Carson, "A multimodal approach to image-derived input functions for brain PET," in *Proc. IEEE Nucl. Sci. Symp. Conf. Rec.*, Oct. 24, 2009, vol. 2009, pp. 2710–2714.

[13] M. Liptrot, K. H. Adams, L. Martiny, L. H. Pinborg, M. N. Lonsdale, N. V. Olsen, S. Holm, C. Svarer, and G. M. Knudsen, "Cluster analysis in kinetic modelling of the brain: A noninvasive alternative to arterial sampling," *Neuroimage*, vol. 21, pp. 483–493, Feb. 2004.

[14] M. Naganawa, Y. Kimura, K. Ishii, K. Oda, K. Ishiwata, and A. Matani, "Extraction of a plasma time-activity curve from dynamic brain PET images based on independent component analysis," *IEEE Trans. Biomed. Eng.*, vol. 52, no. 2, pp. 201–210, Feb. 2005.

[15] R. T. Ogden, F. Zanderigo, S. Choy, J. J. Mann, and R. V. Parsey, "Simultaneous estimation of input functions: An empirical study," *J. Cerebral Blood Flow Metab.: Official J. Int. Soc. Cerebral Blood Flow Metab.*, vol. 30, pp. 816–826, Apr. 2010.

[16] K. Chen, X. Chen, R. Renaut, G. E. Alexander, D. Bandy, H. Guo, and E. M. Reiman, "Characterization of the image-derived carotid artery input function using independent component analysis for the quantitation of [18F] fluorodeoxyglucose positron emission tomography images," *Phys. Med. Biol.*, vol. 52, pp. 7055–7071, Dec. 7, 2007.

[17] A. Hahn, L. Nics, P. Baldinger, W. Wadsak, M. Savli, C. Kraus, W. Birkfellner, J. Ungersboeck, D. Haeusler, M. Mitterhauser, G. Karanikas, S. Kasper, R. Frey, and R. Lanzenberger, "Application of image-derived and venous input functions in major depression using [carbonyl-(11)C]WAY-100635," *Nucl. Med. Biol.*, vol. 40, pp. 371–377, Apr. 2013.

[18] P. L. Bonate. *Pharmacokinetic-Pharmacodynamic Modeling and Simulation*, 2nd ed. New York, NY, USA: Springer Science & Business Media, 2011.

[19] F. O'Sullivan, J. Kirrane, M. Muzi, J. N. O'Sullivan, A. M. Spence, D. A. Mankoff, and K. A. Krohn, "Kinetic quantitation of cerebral PET-FDG studies without concurrent blood sampling: statistical recovery of the arterial input function," *IEEE Trans. Med. Imag.*, vol. 29, no. 3, pp. 610–624, Mar. 2010.

[20] A. Mikhno, F. Zanderigo, R. T. Ogden, M. Mikhno, H. Nagendra, J. J. Mann, A. F. Laine, and R. V. Parsey, "Combining brain imaging data with electronic health records to non-invasively quantify [11 C] DASB binding," in *Proc. IEEE-EMBS Int. Conf. Biomed. Health Informat.*, 2014, pp. 732–735.

[21] N. Ginovart, A. A. Wilson, J. H. Meyer, D. Hussey, and S. Houle, "Positron emission tomography quantification of [(11)C]-DASB binding to the human serotonin transporter: Modeling strategies," *J. Cereb. Blood Flow Metab.*, vol. 21, pp. 1342–1353, Nov. 2001.

[22] A. R. Ferguson, J. L. Nielson, M. H. Cragin, A. E. Bandrowski, and M. E. Martone, "Big data from small data: Data-sharing in the 'long tail' of neuroscience," *Nat. Neurosci.*, vol. 17, pp. 1442–1447, Nov. 2014.

[23] I. Starr, T. G. Schnabel, Jr., S. I. Askovitz, and A. Schild, "Studies made by simulating systole at necropsy. IV. On the relation between pulse pressure and cardiac stroke volume, leading to a clinical method of estimating cardiac output from blood pressure and age," *Circulation*, vol. 9, pp. 648–663, May 1954.

[24] R. D. Mosteller, "Simplified calculation of body-surface area," *N Engl. J. Med.*, vol. 317, p. 1098, Oct. 22, 1987.

[25] S. B. Nadler, J. H. Hidalgo, and T. Bloch, "Prediction of blood volume in normal human adults," *Surgery*, vol. 51, pp. 224–232, Feb. 1962.

[26] M. D. Mifflin, S. T. St Jeor, L. A. Hill, B. J. Scott, S. A. Daugherty, and Y. O. Koh, "A new predictive equation for resting energy expenditure in healthy individuals," *Am. J. Clin. Nutr.*, vol. 51, pp. 241–247, Feb. 1990.

[27] A. S. Levey, J. P. Bosch, J. B. Lewis, T. Greene, N. Rogers, and D. Roth, "A more accurate method to estimate glomerular filtration rate from serum creatinine: A new prediction equation. Modification of Diet in Renal Disease Study Group," *Ann. Intern. Med.*, vol. 130, pp. 461–470, Mar. 16, 1999.

[28] L. A. Stevens, T. D. Nolin, M. M. Richardson, H. I. Feldman, J. B. Lewis, R. Rodby, R. Townsend, A. Okparavero, Y. L. Zhang, C. H. Schmid, A. S. Levey, and C. Chronic Kidney Disease Epidemiology, "Comparison of drug dosing recommendations based on measured GFR and kidney function estimating equations," *Am. J. Kidney Dis*, vol. 54, pp. 33–42, Jul. 2009.

[29] R. T. Ogden, A. Ojha, K. Erlandsson, M. A. Oquendo, J. J. Mann, and R. V. Parsey, "*In vivo* quantification of serotonin transporters using [(11)C]DASB and positron emission tomography in humans: Modeling considerations," *J. Cereb. Blood Flow Metab.*, vol. 27, pp. 205–217, Jan. 2007.

[30] S. Kirkpatrick, C. D. Gelatt, Jr., and M. P. Vecchi, "Optimization by simulated annealing," *Science*, vol. 220, pp. 671–680, May 13, 1983.

[31] M. Gibaldi and D. Perrier, *Pharmacokinetics Second Edition Revised and Expanded*. New York, NY, USA: Marcel Dekker, 1982.

[32] M. M. Graham, "Physiologic smoothing of blood time-activity curves for PET data analysis," *J. Nucl. Med.*, vol. 38, pp. 1161–1168, Jul. 1997.

[33] K.-P. Wong, S. R. Meikle, D. Feng, and M. J. Fulham, "Estimation of input function and kinetic parameters using simulated annealing: application in a flow model," *IEEE Trans. Nuclear Sci.*, vol. 49, no. 3, pp. 707–713, Jun. 2002.

[34] A. Kriplani, D. J. Schlyer, P. Vaska, S. Southekal, S. J. Park, C. L. Woody, S. P. Stoll, S. Junnarkar, and J. F. Pratte, "Feasibility studies for extracting an input function for quantitative positron emission tomography using a wrist scanner," in *Proc. IEEE 33rd Annu. Northeast Bioeng. Conf.*, 2007, pp. 51–53.

[35] A. K. Alstrup, A. M. Landau, J. E. Holden, S. Jakobsen, A. C. Schacht, H. Audrain, G. Wegener, A. K. Hansen, A. Gjedde, and D. J. Doudet, "Effects of anesthesia and species on the uptake or binding of radioligands *in vivo* in the Gottingen minipig," *Biomed. Res. Int.*, vol. 2013, p. 808713, 2013.

[36] E. Kauppila, E. Vanninen, S. Kaurijoki, L. Karhunen, K. H. Pietilainen, A. Rissanen, J. Tiihonen, U. Pesonen, and J. Kaprio, "Influence of serotonin transporter gene polymorphism (5-HTTLPR polymorphism) on the relation between brain 5-HT transporter binding and heart rate corrected cardiac repolarization interval," *PLoS One*, vol. 8, p. e50303, 2013.

[37] E. H. Kang, I. S. Lee, J. E. Park, K. J. Kim, and B. H. Yu, "Platelet serotonin transporter function and heart rate variability in patients with panic disorder," *J. Korean Med. Sci.*, vol. 25, pp. 613–618, Apr. 2010.

[38] B. J. Parker and F. Dagan, "Graph-based Mumford-Shah segmentation of dynamic PET with application to input function estimation," *IEEE Trans. Nuclear Sci.*, vol. 52, no. 1, pp. 79–89, Feb. 2005.

[39] J. E. Mourik, M. Lubberink, U. M. Klumpers, E. F. Comans, A. A. Lammertsma, and R. Boellaard, "Partial volume corrected image derived input functions for dynamic PET brain studies: Methodology and validation for [11C]flumazenil," *Neuroimage*, vol. 39, pp. 1041–1050, Feb. 1, 2008.

[40] Turku-PET-Center. Jan. 2, 2015. *Converting Blood TAC to Plasma TAC* [Online]. Available: http://www.turkupetcentre.net/petanalysis/input_blood-to-plasma.html

[41] R. Hinz, S. Selvaraj, N. V. Murthy, Z. Bhagwagar, M. Taylor, P. J. Cowen, and P. M. Grasby, "Effects of citalopram infusion on the serotonin transporter binding of [11C]DASB in healthy controls," *J. Cereb. Blood Flow Metab.*, vol. 28, pp. 1478–1490, Aug. 2008.

[42] F. Zanderigo, R. T. Ogden, and R. V. Parsey, "Reference region approaches in PET: A comparative study on multiple radioligands," *J. Cereb. Blood Flow Metab.*, vol. 33, pp. 888–897, Jun. 2013.

[43] F. Zanderigo, R. T. Ogden, and R. V. Parsey, "Noninvasive blood-free full quantification of positron emission tomography radioligand binding," *J. Cereb. Blood Flow Metab.*, vol. 35, pp. 148–156, Nov. 5, 2014.

Authors' photographs and biographies not available at the time of publication.